Thermomechanical Relaxation of Vibrationally Excited NO in a Hypersonic Turbulent Boundary Layer

Casey J. Broslawski*
NASA Langley Research Center, Hampton, VA, 23681-2199

Zachary D. Buen†
L3Harris Technologies, Inc., San Leandro, CA, 94577

Ashley N. Moran‡, Madeline A. Smotzer§, Simon W. North¶, Rodney D. W. Bowersox‖
Texas A&M University, College Station, TX, 77843-3141

Bryan J. Morreale**
Lawrence Livermore National Laboratory, Livermore, CA 94550

The effects of thermal nonequilibrium are studied using a DC glow discharge plasma to selectively modify the vibrational temperature of an otherwise cold flow. These experiments were performed at $M = 5.7$ and $Re = 6 \times 10^6/\text{m}$ in the Actively Controlled Expansion tunnel at Texas A&M University on a canonical 2.75° half-angle wedge test article. A ~ 47 W plasma was generated across spanwise electrodes, and removable trips produced either a laminar or turbulent boundary layer. NO planar laser-induced fluorescence (PLIF) quantified the extent of the NO $X^2\Pi$ ($v = 1$) vibrational perturbation due to the plasma and its subsequent interplay with the boundary layer, the first such data of which the authors are aware. NO PLIF measurements were taken at three locations along the test article, and quasi-temperature measurements are reported at each. Despite not quantifiably perturbing the boundary layer, the plasma was shown to alter the NO vibrational temperature profile therein. Independent analysis of the thermodynamics and fluid mechanics of the system suggests each set of physics could explain the results observed near and far from the wall, respectively.

*Research Aerospace Engineer, Aerothermodynamics Branch, MS 408A, AIAA Young Professional Member.
†Optical Engineer.
‡PhD candidate, Department of Chemistry, AIAA Student Member.
§PhD Candidate, Department of Chemistry, AIAA Student Member.
¶Professor and Department Head, Department of Chemistry.
‖Professor, Aerospace Engineering; Senior Associate Dean for Research and CRO; Deputy Director, Texas A&M Engineering Experiment Station; Regents Professor; Holder, Ford I Professorship; AIAA Fellow.
**Flight Engineer, Computational Engineering Division, Strategic Deterrence, AIAA Member

I. Nomenclature

a_1	=	Empirical constant
ACE	=	Actively Controlled Expansion tunnel
A_{21}	=	Einstein A coefficient between States 1 and 2
B_{12}	=	Einstein B coefficient between States 1 and 2
C_{12}	=	Empirical constant
C_D	=	Empirical constant
Da_v	=	Damköhler number
DC	=	Direct Current
E_v	=	Spectral fluence ($J \cdot cm^2 \cdot Hz$)
E^v	=	Vibrational energy at level v
ΔE^{vib}	=	Vibrational energy spacing
ΔE^{ex}	=	Anharmonic vibration constant
X_e	=	Boundary layer edge value
I	=	Current
$ICCD$	=	Intensified Chage-Coupled Device
k, k_f, k_r	=	Reaction rate constant, forward and reverse reactions
k_b	=	Boltzmann constant
K^T	=	Turbulent kinetic energy
l, l_{body}, l_m	=	Length scale, body, mixing
M	=	Mach number
X_m	=	Species
N	=	Number of molecules
n	=	Number density
$N^{Boltz}_{m,v}$	=	Boltzmann population distribution
P, P_o, P', $\overline{P}$	=	Static, stagnation, fluctuating, Reynolds-averaged pressure
P_{pl}	=	Plasma power
$PLIF$	=	Planar Laser-Induced Fluorescence
$pt(T)$	=	A temperature-dependent component of reaction rate constant
Q_{21}	=	Quenching between States 1 and 2
R	=	Ratio of fluorescence signal
X^v, X_v	=	Denotes rotranslational value

R_{eff}	=	Radius of curvature, effective radius of curvature
R_b	=	Ballast resistor
R_c	=	Radius of curvature
$RANS$	=	Reynolds-averaged Navier-Stokes
Re	=	Unit Reynolds number (10^6/m)
$T, T_o, \overline{T}$	=	Rotranslational state or static, stagnation, Reynolds-averaged temperature
u, u^*, u'_{RMS}	=	Velocity, friction velocity, root-mean square velocity fluctuation
t	=	Time
TNE	=	Thermal Nonequilibrium
V	=	Vibrational state
v, v', v''	=	Vibrational energy level
X^v, X_v	=	Denotes vibrational excitation or energy level
V_{pl}, V_{PS}, V_b	=	Plasma, power supply, and ballast resistor voltage
X_w	=	Wall value
x	=	Streamwise coordinate
Y^+	=	Dimensionless wall distance
y	=	Wall normal coordinate
β	=	Nondimensional parameter
$\delta, \delta_{H_o,\ 99.5\%}$	=	Boundary layer thickness, thickness calculated from 99.5% stagnation enthalpy
$\Delta\epsilon_{ab}$	=	The energy spacing between probed A and B transitions
ϵ	=	Dissipation
η	=	Optical transmission efficiency
θ^{vib}	=	Characteristic vibrational temperature
κ	=	Curvature, empirical constant
λ	=	Taylor microscale
ν	=	Kinematic viscosity
ρ	=	Density
τ	=	Shear stress
$\tau_{LT}, \tau_F, \tau_E, \tau_\eta, \tau_\lambda$	=	Landau-Teller, flow, large eddy turnover, Kolmogorov, Taylor microscale timescale
τ^T_{xy}	=	Reynolds stress
χ_m	=	Mole fraction of NO
Ω	=	Collection solid angle

II. Introduction

The high Reynolds numbers and enthalpies experienced during hypersonic flight are capable of producing turbulent flows in thermochemical nonequilibrium. However, reproducing such complex phenomena in ground test facilities and numerical simulations remains a significant challenge. In traditional blowdown wind tunnels, the stagnation temperatures are low enough for the perfect gas assumption to describe the environment; high-enthalpy tests are then reserved for shock-driven or arc-jet facilities. Analogously, in most industry computational packages, one can either run a simulation with thermochemical nonquilibrium and turbulence switched "On" or "Off." This binary approach to complex flow physics precludes all but the most dedicated studies from advancing the field and obfuscates connections between specific flow physics. Recent success has been made by taking a more incremental approach, focusing on two-temperature vibrational excitation in canonical turbulent environments.

Bowersox et al. [1] derived an analytical model for the transport of internal energy flux. In doing so, they identified a direct mathematical link between the vibrational relaxation and turbulence timescales. Although this preliminary work relied on significant assumptions, it connected internal energy and turbulent quantities in a RANS framework.

Fuller et al. [2] conducted an experiment in a subsonic channel flow with decaying mesh turbulence. They used 150 and 300 W radio-frequency glow discharges to vibrationally excite their system of N_2, O_2, and NO ($\sim$ 1% by mass). Optical emission spectroscopy suggested the plasma only weakly heated the gas, but coherent anti-Stokes Raman spectroscopy showed there was significant vibrational excitation of the N_2, and that this excitation decayed along the channel. NO PLIF thermometry measurements revealed a corresponding rise in the rotranslational temperature as vibrational energy was passed into these modes. Chemical kinetics modeling suggested that water vapor present in the ambient environment led to the efficient energy transfer. Particle imaging velocimetry quantified a decrease in Reynolds stress in the presence of the plasma as the increased temperature of the bath gas elevated the flow viscosity. This illustrates a viable mechanism by which vibrational TNE can affect turbulence.

Fujii and Hornung [3] and Wagnild [4] found that when simulating the effect of vibrational nonequilibrium on a single acoustic wave, optimal dampening occurred when the frequency of the wave matched the vibrational relaxation timescale. Neville et al. [5] extended this concept to compressible, isotropic turbulence and to turbulent shear layers [6]. Here the researchers tuned the Mach numbers as well as the ratio of the large eddy and vibrational relaxation timescales as described by the Damköhler number Da_v. In all cases, damping occurred when changes in the vibrational energy lagged behind the turbulent fluctuations in rotranslational temperature such that energy could be stored in and released from vibrational modes during corresponding peaks and troughs in rotranslational temperature.

Khurshid and Donzis [7] used direct numerical simulations to study the effect of TNE on decaying turbulence. They produced β, a nondimensional parameter, which effectively added the degree of initial TNE to Da_v. As in Refs. [5, 6], this allowed a study of the full spectrum of flows, from vibrationally ($\beta \ll 1$) to mechanically ($\beta \gg 1$) frozen, but improved the fidelity by considering the initial condition. They found that for mechanically slow flows, as the initial

TNE increased (increasing β), the more rapid the impact on the flow, though an asymptotic limit existed. Khurshid and Donzis [7] supported the energy exchange mechanism identified by Fuller et al. [2] and expanded upon it. They also noted that because of the temperature dependence of the vibrational relaxation timescale, it is possible to have transient cases of vibrationally cold flow. Furthermore, due to the same nonlinear relationship between temperature, the vibrational relaxation time constant, and mean vibrational energy for mechanically and especially vibrationally frozen flows, Donzis and Maqui [8] note that turbulent flows can store a greater portion of energy in vibrational modes than laminar ones at analogous conditions such that $\overline{T}^v_{turb} > \overline{T}^v_{lam}$.

The effect of TNE in a hypersonic blowdown facility was experimentally studied at The Ohio State University [9]. Two types of electric discharges were used to modify the internal energy modes of N_2 and O_2 molecules. Downstream of the plasma, rapid relaxers were injected to further control the internal energy modes in TNE. A suite of optical diagnostic techniques were used to study the nonequilibrium flowfield produced and to assess flow modeling calculations, including optical emission spectroscopy and laser diagnostics. The most relevant measurements to the current study report used NO PLIF to measure the rotranslational and vibrational temperatures around a cylindrical model [9]. Even without NO injection, the plasmas in the plenum produced sufficient NO to allow NO PLIF flow visualization of the test article bow shock. Subsequent coherent anti-Stokes Raman spectroscopy measurements showed there was no vibrational relaxation across the cylinder bow shock [10].

The present work demonstrates the introduction and measurement of vibrational TNE in a hypersonic boundary layer along a flat plate test article through the use of a DC glow discharge plasma. Qualitative NO PLIF measurements identified trends in the vibrational temperature through the boundary layer at three streamwise locations along the plate. A trip insert induced turbulence in the boundary layer to provide insight into the interplay between turbulence and TNE. The trends in the experimental results were explored using basic thermodynamics and fluid mechanics principles.

III. Experimental Facilities & Diagnostics

A. Actively Controlled Expansion (ACE) Tunnel

All experiments were conducted in the ACE Tunnel [11, 12], an open-circuit blowdown facility with an adjustable nozzle that allows $M = 5 - 8$. To achieve the requisite pressure differential, air is compressed by two compressors and stored at 17.24 MPa in a 23.2 m^3 tank; the air is filtered for particles > 1 µm and dried to a dew point of 233.15 K. This tank supplies both the plenum pressure for the tunnel, as well as a two-stage air ejector, which produces a vacuum of 530 Pa to further improve the pressure differential. Before running, the facility is preheated to nominally 430 K using a 0.5 MW electrical resistance heater. All air sent into the tunnel is passed through a redundant 1-µm filter.

A sketch of the ACE Tunnel is shown in Fig. 1 and nominal test conditions for the current work are shown in Table 1. The test section is 35.88 cm wide, 23.18 cm tall, and 66.04 cm long and has a series of three 12.70 cm optical ports on

both the top and bottom surface; customizable doors on either side of the test section allow further optical access. All windows used in this campaign were fused silica to allow for high (> 90%) UV transmission over the wavelengths of interest. A stainless steel table with a breadboard tabletop and optical rail cage surrounds the test section to support all diagnostic hardware without interference from the tunnel vibrations.

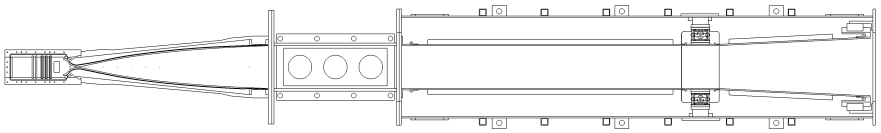

Fig. 1 Side-view sketch of the ACE tunnel; flow travels from left to right.

Table 1 Nominal test conditions for the ACE facility for the experiments conducted.

M	Re (10^6/m)	P_o (kPa)	T_o (K)	P (Torr)	T (K)	ρ ($\frac{\text{kg}}{\text{m}^3}$)	$\frac{P'_{RMS}}{\overline{P}}$ (%)
5.70	6.00	496.42	430	3.23	57.35	2.61	1.5
±0.05	±0.25	±20.68	±15	±0.13	±2.00	$\pm 0.2 \times 10^{-2}$	±0.25

1. Flow Seeding

This study seeded NO into the plenum to enable NO PLIF in the ACE tunnel test section. A seeder designed for continuous flow produced a homogenized and thermalized NO environment. Pure NO (99.95%) and N_2 (99.999%) were mixed using a proportional-integral-derivative algorithm controlling mass flow controllers. A 15% NO mix provided sufficient seeding for a workable signal-to-noise ratio and minimized cost. The mix was stored in two stainless steel ballast tanks with a total capacity of 7571 cm^3. Pressure transducers monitored the reservoir and delivered static pressure measurements.

The settling chamber was modified to support the injection of NO into the flow via a stainless steel seeder. A parameterized study of gas seeders (opening area, orientation, size, etc.) is included in Refs. [13, 14]. A 0.953 cm pipe crimped into a ~2:1 aerodynamic shape was placed ~2.54 cm upstream of the settling chamber aerogrids and meshes to reduce its wake effects and to more homogeneously distribute the gas. A single 1.59 mm gas exit orifice was positioned 66.7 mm from the settling chamber floor. The seeder orifice was strategically placed such that the bulk of the gas was sent into the region of interest on the top half of the test article. The test article was positioned 2.54 cm below the center of the test section for the same reason.

The resulting distribution of NO, measured using PLIF flow visualization, was approximately elliptical with major (top-down) and minor (spanwise) axes of 120 and 60 mm, respectively. During a nominal run (see Table 1) the seeder would choke if P_o, NO > 939.693 kPa [15] and the NO ballast tanks would fall from 1241.06 to 551.581 kPa; the effect of this decrease was not detectable in the PLIF data. The mass flow rate of the ACE tunnel was 1.8766 kg/s while that for the seeder was 4.5858 to 2.0381×10^{-3} kg/s. Using the Ideal Gas Law, from Table 1

n_{ACE} = 5.43 $\times$ 10^{17}/cm^3. Assuming all NO was concentrated in the ellipse, for the 15% NO mix used here, then n_{NO} = 9.1360 to 2.5060 $\times$ 10^{14}/cm^3. Thus, the resulting concentration of NO was 0.1683 to 0.0462%. It is noted that Buen [14] estimated the local concentration of NO by modeling the decay of the measured NO fluorescence lifetime, finding a ~100:1 ratio between the injected gas concentration and the concentration measured in the test section, validating the a priori methodology used here.

B. Test Article

The test article was designed to be a canonical testbed for a variety of zero pressure gradient boundary layer studies. Its design built upon over a decade of analogous testing in the ACE tunnel [16–18], and a detailed description can be found in Ref. [19]. The present configuration was a 2.75° half-angle wedge 0.216 m wide and 0.508 m long. The half-angle was set to allow sufficient material to move the trips, electrodes, and windows as near the leading edge as possible without deviating significantly from true zero pressure gradient behavior [20]. These dimensions allowed a test area ±25.4 mm about the centerline while not exceeding the blockage limits of the ACE tunnel. Three support struts minimized vibration during testing and controlled pitch and roll to < 0.1°. A section view CAD model of the test article in the test section is shown in Fig. 2. Measurements were taken along the centerline with the image centers approximately 115 ("Front"), 260 ("Middle"), and 405 mm ("Back") from the leading edge.

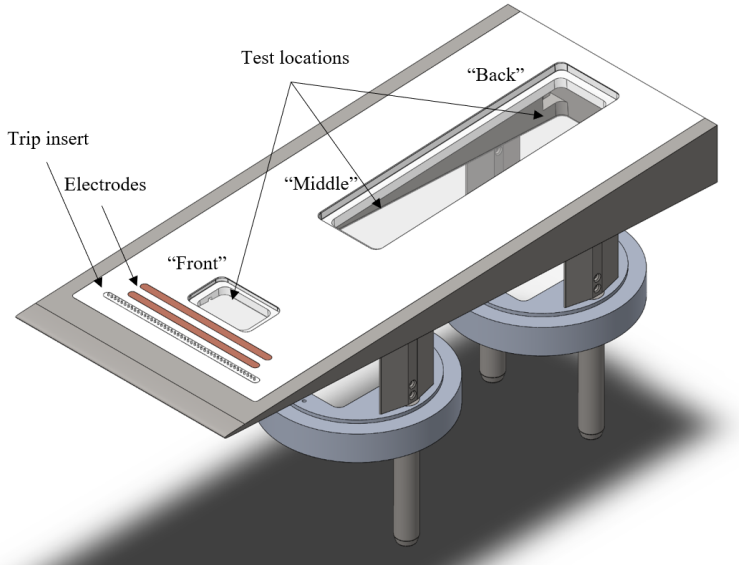

Fig. 2 Isometric CAD view of the test article with key features annotated.

An insert made from PEEK, a material chosen to provide the requisite electrical and thermal resistivity, was fitted into the polished (32G, 0.81 µm [19]) wedge stainless steel frame. The PEEK insert was machined as a single piece to remove any junctions that could perturb the flowfield. Custom-made fused silica, antireflective coated windows (transmissivity > 90%; reflectivity < 0.5%) were mounted along the centerline to allow laser measurements through the

boundary layer at different test locations. All junctions with the top surface were hermetically sealed to prevent suction or blowing in the test area.

Following Leidy [17], special care was taken in designing the leading edge to produce stable stagnation at the nose [21] and remove a receptivity source at the junction of the nose and wedge [22]. A sixth-order polynomial $P(x) = Ax^6 + Bx^5 + Cx^4$ was generated that met three conditions at the junction: 1) $P(x_{junct} = 0.082 \text{ in}) = 0.813$ in 2) $P'(x_{junct}) = \frac{1}{\tan(2.75°)}$ 3) $P''(x_{junct}) = 0$ to maintain the curvature $\kappa = \left|\frac{P''}{(1+P'^2)^{3/2}}\right| = 0$. The result was, in inches, $P(x) = 4.2809 \times 10^6 x^6 - 1.1188 \times 10^6 x^5 + 8.0936 \times 10^4 x^4$. Because the radius of curvature $R_c = 1/\kappa$ is variable for polynomials, the corner $P(x_{R_{c,\,min}})$ of the box-like sixth-order polynomial is provided as an effective radius of curvature. Here $R_{eff} = 0.318$ mm, which falls between the 0.366 mm from Ref. [17] and 1.400 mm from Ref. [18] (1.25×10^{-2} in, 1.44×10^{-2} in, and 5.51×10^{-3} in, respectively)

1. DC Glow Discharge

A DC glow discharge was used to introduce TNE in a controllable, incremental manner such that only some vibrational modes needed to be considered at any one time. Much of the design of the plasma system followed from the $M = 5$ blowdown tunnel experiments on a laminar flat plate boundary layer described in Refs. [23–29]. These authors sought to use a glow discharge plasma as an actuator, directly affecting the boundary layer through heating and pressure effects. Here such perturbation was undesirable as the goal was to isolate and study the effect of TNE on an unperturbed turbulent hypersonic boundary layer; success in this regard is described in Ref. [19].

A 300 W (100 mA, 3000 V) power supply produced the plasma; the switching power supply ran a voltage-limited configuration. The power supply output voltage and current were stored for subsequent analyses. From these parameters and the known $R_b = 10.03 \pm 0.09$ kΩ chassis mount ballast resistor on the high-voltage (anode) leg of the circuit, one could calculate [30]: voltage drop across the ballast resistor (V_b); plasma voltage ($V_{pl} = V_{PS} - Vb$); and plasma power from Ohm's Law ($P_{pl} = IV_{pl} = 47$ W [19]). The ballast resistor was connected to the high-voltage (anode) and the low-voltage (cathode) electrode was grounded to the wind tunnel before returning to the power supply.

The polished copper electrodes were rounded rectangles 13.34 cm long and 0.635 cm wide. Their edge-to-edge spacing was 0.635 cm; a buffer 4.5 times this distance was maintained between the electrodes and all metal surfaces to prevent accidental ignition. To encourage a normal glow discharge (see Refs. [31–33]), the electrode areas were kept as small as possible while still preventing any edge effects in the region of interest. The interelectrode spacing was set experimentally as Paschen's curve could not accurately predict the thermal and temperature gradients present in the hot tripped boundary layer. The polarity, with the anode upstream of the cathode, was also set following experimentation. Further details of the system are provided by Broslawski et al. [19].

2. Trips

The ACE tunnel Reynolds number and density necessitate trips to produce a turbulent boundary layer on a flat plate. Berry et al. [34] developed diamond-shaped trips for an analogous experiment, and this configuration was tested successfully in the ACE tunnel [16, 17] so the same geometry was used for this study. The diamond trips had heights, width (corner-to-corner), and spacing that could be scaled, following Berry et al. [34], by the boundary layer total enthalpy thickness $\delta_{H_o,99.5\%}$. For the present study, $\delta_{H_o,99.5\%}$ was predicted for a laminar boundary layer using the self-similar portion of the in-house RANS code discussed below; this preliminary work used an early version of the code, but any changes did not change the efficacy of the trips. Ultimately $\delta_{H_o,99.5\%} = 1.71$ mm was used. Because the objective was solely a fully developed turbulent boundary layer with minimum wake effects, a trip sizing study was conducted to find the best trip for the specific test environment. A parameterized trip sizing study is provided in Ref. [19], but to summarize the selected option was [height, width, spacing] = $\delta_{H_o,99.5\%}[1.5,\ 2,\ 4]$ = [2.57, 3.42, 6.84] mm. This configuration produced a transitional boundary layer in the first test location and a fully developed turbulent boundary layer by the second and third test locations. The trips were made using stereolithography rapid prototyping in-house from Formlabs' proprietary "Grey Pro" resin. They were centered about the test article centerline such that a trip was in the middle of the span, where all subsequent data were collected.

C. NO Planar Laser-Induced Fluorescence

The PLIF thermometry measurements required two laser systems. The 532 nm second harmonic output of an injection seeded Nd:YAG laser was used to pump a dye laser. The dye laser systems for the NO $A^2\Sigma^+\,(v'=0) \leftarrow X^2\Pi_{1/2}\,(v''=0)$ transition and the NO $A^2\Sigma^+\,(v'=1) \leftarrow X^2\Pi_{1/2}\,(v''=1)$ transition used solutions of Rhodamine 640 in ethanol and a mixture of Rhodamine 640/610 in methanol, respectively, to produce output tunability in the 600 – 630 nm range. The residual 355 nm of the Nd:YAG laser was mixed with the tunable output of the dye laser in a sum-frequency mixing unit to produce the requisite 223 – 226 nm light at ~2.5 mJ/pulse with linewidths of 0.08 cm^{-1} [35]. Additional information on the laser system can be found in Refs. [14, 35]. The beams were directed into the tunnel, top-down through the boundary layer and test article, using 225 nm dichroic mirrors. The laser beams were directed through a 300 mm cylindrical plano-concave lens and a 500 mm cylindrical plano-convex lens into ~ 1.5 cm wide and ~ 800 µm thick overlapping sheets. The beams were focused 30 mm above the surface of the plate to reduce scatter and were aligned at the spanwise centerline of the test article. All lenses and tunnel windows were ultraviolet-grade fused silica.

Each laser was tuned to probe different vibrational states. One laser probed the NO $A^2\Sigma^+\,(v'=0) \leftarrow X^2\Pi_{1/2}\,(v''=0)$ transition and the second probed the NO $A^2\Sigma^+\,(v'=1) \leftarrow X^2\Pi_{1/2}\,(v''=1)$ transition. In both cases, the J 4.5 rotational state of the Q_{21}/R_1 branch was probed as its signal was relatively invariant to the rotational temperature change across the boundary layer. During the tests, the $\text{NO}^{v=1}$ transition was probed first because it was assumed relaxation from NO $A^2\Sigma^+$ (v'=1) to NO $X^2\Pi$ (v"=0) would be negligible compared to the ground $X^2\Pi$ (v"=0) state. This also allowed for

minimization of thermal perturbations caused by the potential production of $NO^{v=1}$ from NO_2 photodissociation. The $NO^{v=0}$ population was probed 500 ns after the $NO^{v=1}$ population.

The signal was collected using two ICCD cameras. Air cooling the cameras to 253.15 K and background subtracting the frames improved signal-to-noise. The 1024 $\times$ 1024 pixel arrays of the camera were 2 $\times$ 2 binned to match the repetition rate to the 10 Hz laser repetition rate. Even so, using ultraviolet-grade 100mm F/2.8 focusing lenses and extension tubes a spatial resolution of $\sim$ 100 µm was maintained across the approximately 20 $\times$ 20 mm field of view. The cameras were placed on opposing sides of the test section and were aligned onto the same region of interest using a 1 mm $\times$ 1 mm grid card. Both cameras were intensified 100 times, and the time delay between images was ~500 ns, so chosen to allow thermalization with minimal streamwise movement (~4.25 pix in the ~850 $\frac{\text{m}}{\text{s}}$ freestream). The camera imaging the $NO^{v=0}$ was nominally gated for 3 ns and the camera imaging the $NO^{v=1}$ was nominally gated for 100 ns.

The theory for two-line thermometry data reduction is well-summarized by Seitzman and Hanson [36]. For a steady state system operating in the linear fluorescence regime stimulated via a broadband laser profile the number of photons N_p collected by a detector over 4π steradians is provided in Eq. 1.

$$N_p = \eta \frac{\Omega}{4\pi} f_1(T) \chi_m n V_c B_{12} E_v \frac{A_{21}}{A_{21} + Q_{21}} \tag{1}$$

Here $f_1(T)$ is the fractional population of the lower laser-coupled state in the absence of the laser field, χ_m is the mole fraction of NO, and n is the total number density. For energy transfers between States 1 and 2, Q_{21} captures quenching via intra- and intermolecular collisions, B_{12} captures absorption and stimulated emission, and A_{21} captures spontaneous fluorescence. Following a derivation included in Ref. [36], for two frames "A" and "B" probing the same rotational state at different vibrational energy levels (vibrational thermometry, vice versa for rotranslational thermometry), one arrives at Eq. 2.

$$R = \frac{N_{p,a}}{N_{p,b}} = C_{12} * \exp\left(-\frac{\Delta\epsilon_{ab}}{k_b T}\right) \tag{2}$$

Because R is always measured, the empirical C_{12} is calibrated by solving Eq. 2 in a region where T is known, such as the freestream. However, it will be shown shortly that significant vibrational nonequilibrium is expected between the NO and air, complicating estimation of the empirical C_{12} and thereby the vibrational temperature. For this reason, quantitative vibrational temperatures cannot be reported, only those relative temperatures implied by R and scaled by the edge condition R_e. Fortunately, this is sufficient for determination of relevant trends. R_e is determined by averaging the top 2.5 mm, or ~10%, of the profile. No correction is made for vibrational excitation across the bow shock owing to the weak nature of the oblique shock, low Mach number and temperatures, and lack of observed vibrational temperature jump in analogous experiments [9].

Profiles of R will be calculated by averaging all $100 - 200$ frames collected during a single run before horizontally

averaging across the span. As the relevant region of interest in each image is < 10 mm wide, minimal boundary layer growth is expected, permitting the horizontal averaging. Note from the relationship between R and T in Eq. 2, as the temperature rises, the signal ratio will increase as well, and *vice versa*. Therefore, for simplicity "signal ratio" and "temperature" will be used interchangeably in the analyses herein. However, because the relationship is nonlinear, one must be cautious when inferring relative changes in a temperature from a profile of the signal ratio. Error is approximated by calculating the standard deviation of data across each row in the averaged image; this error is deemed forgiving as it does not account for the decrease in signal near the wall, reflections, the averaging of the frames, etc., but it does provide a measure of the consistency of each image and the success of ensemble-averaging the turbulent images in homogenizing the signal.

IV. Numerical Approach

A. Chemical Kinetics Model

A methodology was developed following Ref. [37] to calculate the evolution of the vibrational temperature of a mixture of N_2, O_2, and NO from a known initial condition and their subsequent rotranslational temperature, pressure, and time. This technique allowed estimation of the freestream T^v_{NO}. The goal with this simple methodology is not precise estimation of T^v_{NO}, but instead to show that it is indeed not frozen in the nozzle, and by extension should not be frozen in the boundary layer of the test article. It is this variability that inhibits quantitative scaling of the vibrational temperature profiles according to Eq. 2 and limits this report to qualitative analyses. It is understood that if a vibrational temperature profile was available near the leading edge of the plate to provide an initial condition and rotranslational temperature data, either via rotranslational PLIF thermometry or CFD, was similarly provided throughout the entire domain, this same 1-D formulation could be extended to a 2-D boundary layer solver by independently solving the row of points at a fixed height above the plate

The gas was assumed to be in thermal equilibrium at the throat of the ACE tunnel and rotranslational temperature and pressure were taken from the nozzle design code. The data were interpolated via $\Delta x = u\Delta t$ with $\Delta t = 1 \times 10^{-9}$ s in an attempt to resolve the rapid chemical reactions at a reasonable computational cost. The methodology outlined herein is greatly simplified and relies on significant approximations, but it is this very simplicity that makes it tractable while providing enough fidelity for a first-order view of relevant trends.

A series of nine V-T energy exchange reactions and three V-V energy exchange reactions were considered for this model to include all the energy exchange reactions between N_2, O_2, and NO. In addition to using additional sources to provide separate constants for each of the nine V-T reactions, Hsu [37] considered the additional chemical species CO_2 H_2O, but these complexities were avoided for this demonstration. Furthermore, the rate constants provided are extrapolated outside of their intended temperature regime as necessitated by the dearth of data available for cold

hypersonic flows engendered by blowdown wind tunnels; this same limitation may frustrate even industrial CFD packages, making their use for estimating $T^v_{e,\,NO}$ impractical. The reactions and their corresponding rate constants are shown in Table 2.

Table 2 Collisional reactions for vibrational relaxation.

Number	Reaction	Forward Rxn. Constants [38]
1	$N_2^{v=1} + O_2{}^{v=0} \leftrightarrow O_2^{v=1} + N_2{}^{v=0}$	$k(T) = \exp\left(-124.0T^{-\frac{1}{3}} - 22.50\right)$ [cm^3/s]
2	$N_2^{v=1} + NO^{v=0} \leftrightarrow NO^{v=1} + N_2{}^{v=0}$	$k(T) = \exp\left(-86.35T^{-\frac{1}{3}} - 21.60\right)$ [cm^3/s]
3	$NO^{v=1} + O_2{}^{v=0} \leftrightarrow O_2^{v=1} + NO^{v=0}$	$k(T) = \exp\left(-62.46T^{-\frac{1}{3}} - 22.35\right)$ [cm^3/s]
4-6	$N_2^{v=1} + (N_2, O_2, NO)^{v=0} \leftrightarrow N_2{}^{v=0} + (N_2, O_2, NO)^{v=0}$	$pt(T) = \exp\left(234.9T^{-\frac{1}{3}} - 25.89\right)$ [atm · s]
7-9	$O_2^{v=1} + (N_2, O_2, NO)^{v=0} \leftrightarrow O_2{}^{v=0} + (N_2, O_2, NO)^{v=0}$	$pt(T) = \frac{T\exp\left(166.3T^{-\frac{1}{3}} - 33.32\right)}{1-\exp(-2240/T)}$ [atm · s]
10-12	$NO^{v=1} + (N_2, O_2, NO)^{v=0} \leftrightarrow NO^{v=0} + (N_2, O_2, NO)^{v=0}$	$pt(T) = \frac{T\exp\left(33.20T^{-\frac{1}{3}} - 25.00\right)}{1-\exp(-2700/T)}$ [atm · s]

The overall strategy is to estimate the initial population fractions of the gases, then observe how they change due to the twelve included reactions. For example, consider Reaction 3 with forward and reverse reaction rates of k_f and k_r, respectively. The rate of change in the concentration (number density) of $NO^{v=1}$ is $\frac{d[NO^{v=1}]}{dt} = -k_f[NO^{v=1}][O_2] + k_r[NO][O_2^{v=1}]$. One can repeat this calculation for all twelve reactions and calculate a cumulative $\frac{d[NO^{v=1}]}{dt}$, and so on for $\frac{d[N_2^{v=1}]}{dt}$ and $\frac{d[O_2^{v=1}]}{dt}$. The forward reaction rate constants were calculated from $k_{VT,v=1} = k_bT/\left(pt(T)\left[1 - \exp\left(-\frac{\theta_m^{vib}}{T}\right)\right]\right)$ where $\theta_m^{vib} = \frac{\Delta E_m^{vib}}{k_b}$ and the constants $pt(T)$ in Table 2 were taken from Candler et al. [38]. The same source provided analogous equations for $k_{VV,v=1}$. The reverse reaction rates were calculated from detailed balance $k_r = k_f \exp\left(-\frac{\theta_m^v}{T}\right)$. For N_2, O_2, and NO, respectively, ΔE_m^{vib} = 2358.57, 1580.19, and 1904.04 cm^{-1} [39]. Note that these reaction rate constants are applicable only to exchanges between $v = (0, 1)$, and that they are being applied outside of their normal temperature range due to the uniquely cold environment for vibrational excitation.

In order to estimate the initial population of $v = 1$, the code assumed each species m was in thermal equilibrium with itself. The energy level for the first twenty vibrational levels v was found from $E_m^v = \Delta E^{vib}(v + 0.5) - \Delta E^{ex}(v + 0.5)^2$ where ΔE^{ex} was 14.324, 11.98, and 14.1 cm^{-1} for N_2, O_2, and NO, respectively. The population fractions of each level were found by dividing the Boltzmann population distributions $N_m^{v,\,Boltz} = \exp\left(-\frac{E_m^v}{k_bT}\right)$ by the sum over all v. The number densities for each species came from the Ideal Gas Law $N_m = P/k_bT$, and so $N_m^v = n_m^{v,\,Boltz}N_m$. For all subsequent streamwise locations, the changes in population due to the reactions were calculated followed by the population fractions n_m^v from $N_m^v/\Sigma_{m=1}^3\Sigma_{v=0}^1 N_m^v$. This restricted the code to low-temperature applications as it neglected significant population of the $v = 2 - 19$ energy levels, but for the ACE tunnel environment and rate constants available, there was little to lose. Finally, with the population of each species known, the Boltzmann equation provided $T_m^{vib} = -\Delta E_m^{vib}/\left(k_b \ln\left[N_m^{v=1}/\left(N_m^{v=0} + N_m^{v=1}\right)\right]\right)$ where $\Delta E_m^v = E_m^{v=1} - E_m^{v=0}$ was 4.6280×10^{-20}, 3.0912×10^{-20},

and 3.7260×10^{-20} J for N_2, O_2, and NO, respectively; here the anharmonicity-corrected values of E_m^v were used.

The results in the nozzle of the ACE tunnel are shown in Fig. 3. The initial condition is provided by assuming thermal equilibrium at the nozzle throat, where static temperature of 358 K is found by isentropic acceleration of the flow from the settling chamber. The concentration of the NO was 0.15%, the estimated amount injected for the corresponding experiments [19]. The small areas of constant T^r (eg.- ~ 0.2 m) are assumed to be from interpolation error or reflected expansion waves in the nozzle and had negligible impact on the final result. It is clear N_2 and O_2 are indeed frozen, while the NO reaches 153.7 K. Thus, the flow can be modeled as a three-temperature system, with $T^r \neq T^v_{N_2,\,O_2} \neq T^v_{NO}$. As expected, the majority of the NO relaxation occurs near the nozzle throat, where the temperature, and thus reaction rates, were the highest and the mean free path was the shortest. Indeed, the NO is rotranslationally thermalized with the bath gas for the first 1 cm downstream of the throat. Further analysis of the reaction rate kinetics and their effect on the flow is included in subsequent sections, but from this example it is clear NO is in vibrational TNE in the freestream and a freestream temperature cannot reliably be provided.

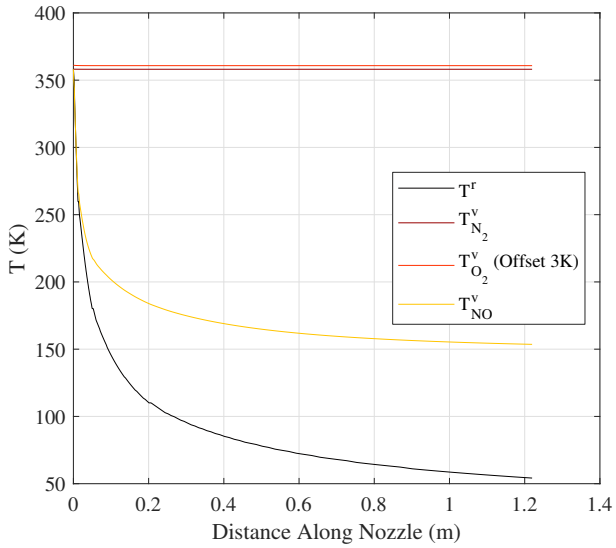

Fig. 3 Simulated temperatures from the ACE nozzle throat to the test section; $T^v_{O_2}$ offset for clarity.

B. US3D Simulation

Proper estimation of thermodynamic mechanisms requires accurate measurement of the rotranslational temperature. In lieu of experimental measurements, here the US3D CFD package [40] provided these data, which is appropriate for such a simple geometry. To that end, a computational mesh was produced from a digital model of the test article using the commercial program Pointwise® (now Cadence®). The input flow conditions nearly matched those in Table 1 ($M = 5.7, T = 58$ K, $\rho = 2.56 \times 10^{-2}$ $\frac{\text{kg}}{\text{m}^3}$) with the post-shock conditions approximated from the equations in Ref. [41]; any discrepancies between these conditions and those in Table 1 are attributed to rounding errors and are deemed

inconsequential. The bow shock set the upper edge of the computational domain. The grid consisted of a single block with 420 nodes in the streamwise and 150 nodes in the wall normal directions, respectively; a single node in the spanwise direction satisfied the requirement of the code for 3-D grids. Streamwise nodes were clustered near the blunt leading edge and wall normal nodes were clustered near the wall according to a hyperbolic tangent distribution with a first cell height of 1×10^{-7} m. This provided, for turbulent cases, $Y+ < 1$. In order to test for grid convergence, the maximum heating under turbulent conditions was compared between grids refined globally by 1.5 times. The results showed agreement $< 3\%$ between the "Medium" and "Fine" grids, thus, the former was used.

The simulation was run using a single temperature and species, which was acceptable given the low concentration of injected NO and vibrational freezing of N_2 and O_2. The compressible Reynolds-averaged Navier Stokes equations were solved using a Modified Steger-Warming inviscid flux scheme ($O(\Delta x, y^2)$) with DPLR implicit time integration to drive the problem to a steady state. The curved bow shock, which defined the inlet of the domain, was given a Dirchlet boundary condition, the side boundary conditions were viscous isothermal (350 K) slip walls, and the outlet was given an extrapolation boundary condition. The convergence criteria was a reduction of 12 orders of magnitude in the initial density residual. Turbulent simulations used the Spalart-Allmaras (SA) model [42], a popular choice in industry and academia [43]. Eddy viscosity was enabled as the start of the domain as opposed to somehow predicting transition due to the physical trips.

The temperature boundary layer results are provided for the "Front" and "Back" test locations in Fig. 4. These data will be used to estimate reaction rate and vibrational relaxation time constants through the boundary layer at these locations.

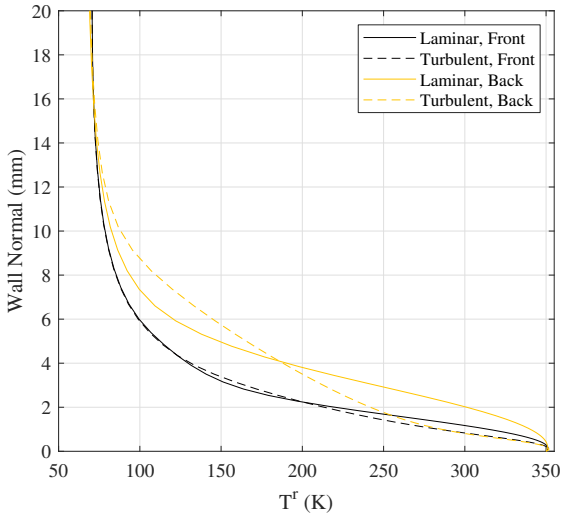

Fig. 4 US3D simulations of the boundary layer rotranslational temperature.

V. Results

The results are presented to provide a narrative in four parts. The first portion covers 2-D images and parameters concerning the boundary layer in general to provide context for subsequent analyses. These analyses begin with the simplest case of the laminar boundary layer without the plasma to ignore the relatively straightforward fluid dynamics and instead focus on the thermodynamic analysis. Mixing is included in the subsequent subsection to substantiate an investigation of the thermal and mechanical timescales present in the domain. Finally, all information is synthesized when the results including plasma excitation of NO are introduced. Understand that here an emphasis is placed on qualitative trends as they are sufficient to substantiate a proposed explanation of the complex thermomechanical relaxation mechanisms present in the problem.

A. Raw PLIF Data

Representative single shot raw fluorescence images are provided in Figs. 5 and 6 for the laminar and turbulent cases, respectively. These data reflect the raw signal from probing the vibrationally excited transition NO $A^2\Sigma^+$ $(v' = 1) \leftarrow$ $X^2\Pi_{1/2}$ $(v'' = 1)$ as this is more relevant than the corresponding vibrationally cold image. All images show a decrease in signal approaching the wall as the density drops due to the hot wall thermal boundary layer. The decay in signal is the primary source of uncertainty throughout the boundary layer [14]. This is partially compensated by the vibrational excitation due to the plasma, best exemplified nearest the electrodes in Figs. 5(b) and 6(b). The longevity of the excited NO is evident from Fig. 5, where even though there is some signal lost along the plate due to boundary layer growth and vibrational relaxation of NO, both mechanisms that will be explored shortly, there is still a clear difference between the plasma "Off" and "On" cases at the "Back" test location, evinced by Figs. 5(e) and 5(f), respectively. The efficacy of the trips is evinced in the turbulent images, which demonstrate the chaotic nature, eddies, and varying spatiotemporal scales present in turbulent boundary layers. The turbulent mixing obfuscated the effect of the plasma, so there is only a clear difference between the plasma "Off" and "On" cases just downstream of the trips in Figs. 6(a) and 6(b), respectively, because the flow is not fully turbulent. Some reflections at the wall are noted in Fig. 6(f).

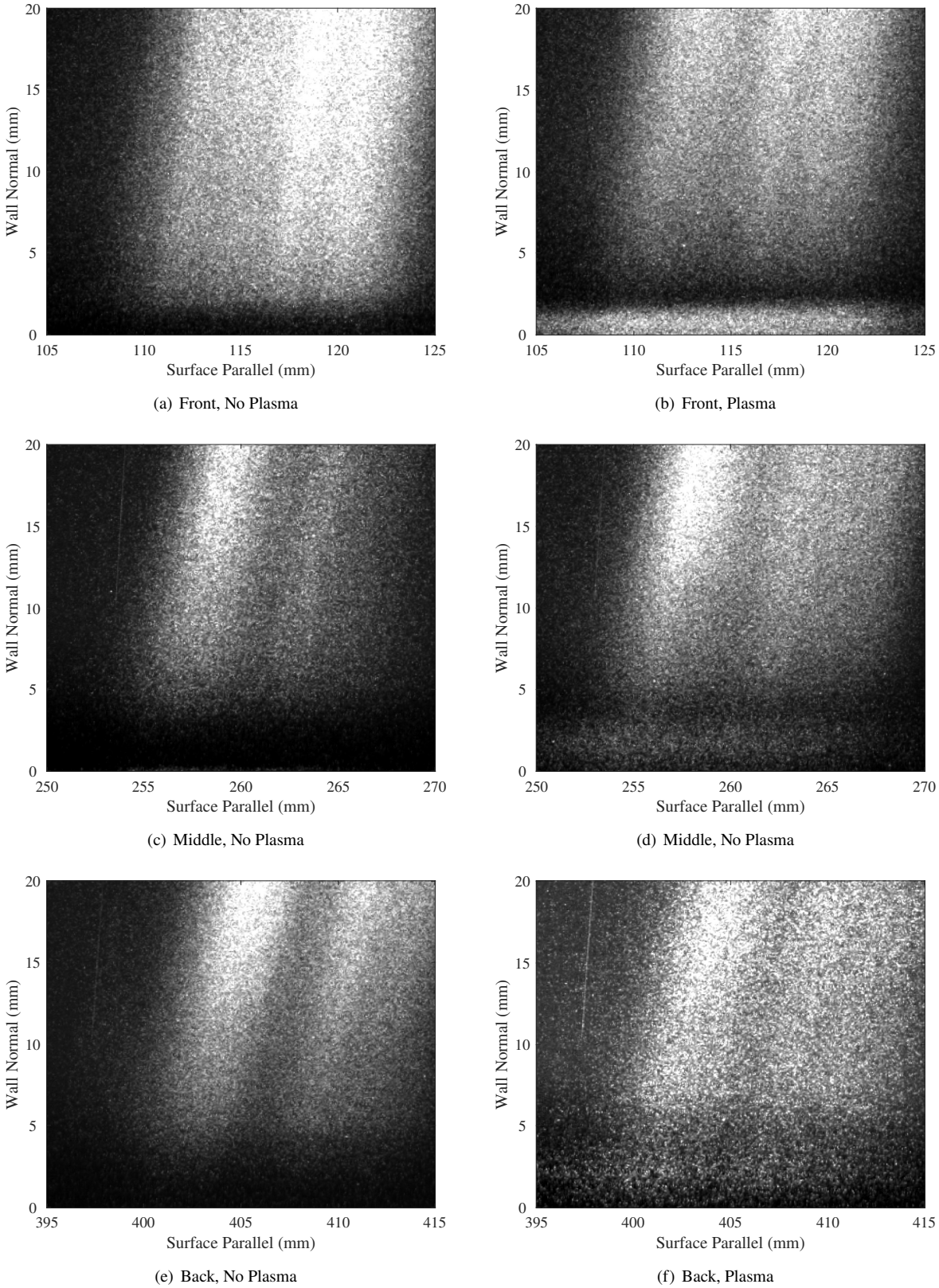

(a) Front, No Plasma

(b) Front, Plasma

(c) Middle, No Plasma

(d) Middle, No Plasma

(e) Back, No Plasma

(f) Back, Plasma

Fig. 5 Sample raw fluorescence images, laminar boundary layer; flow is from left to right.

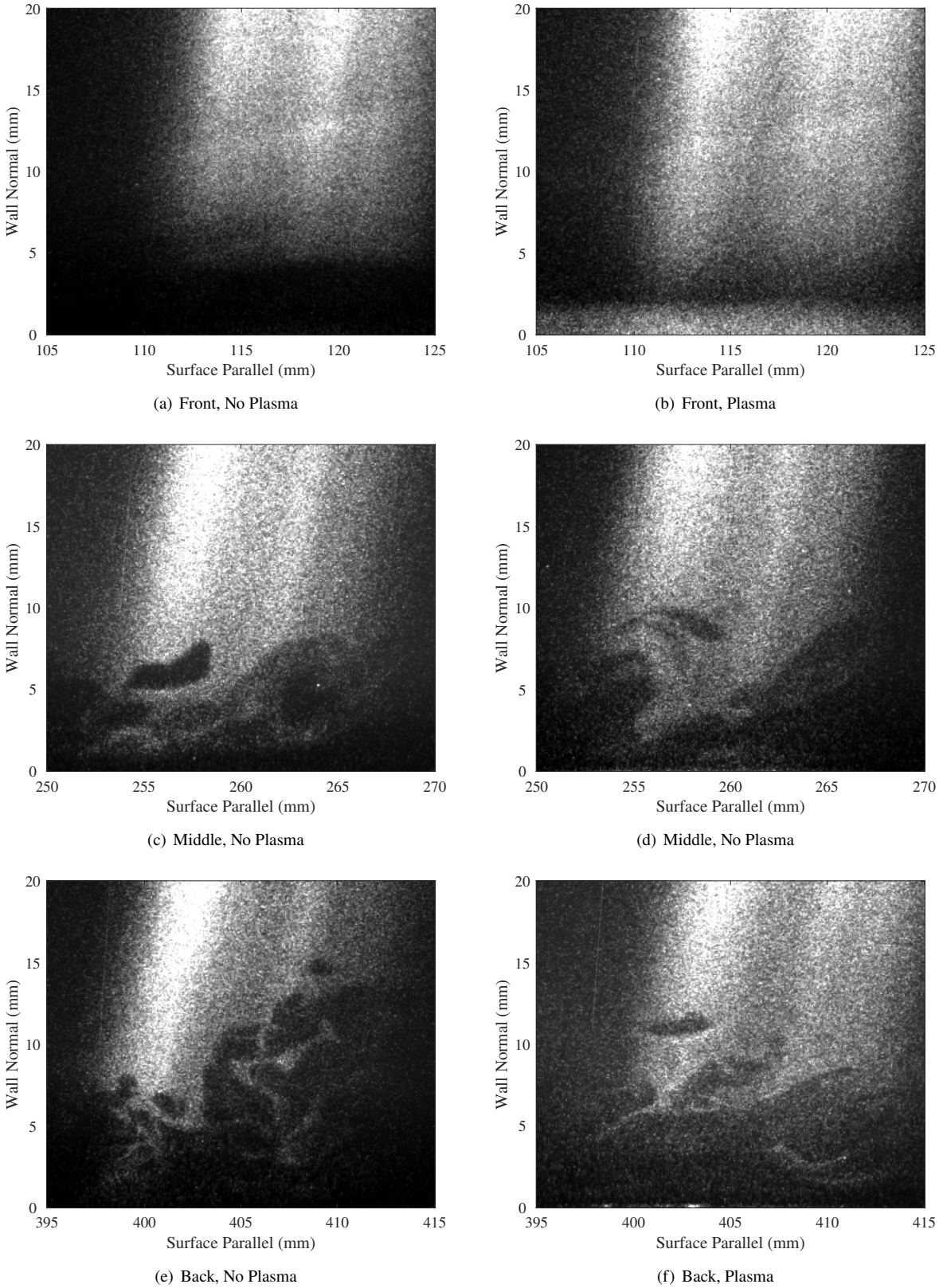

(a) Front, No Plasma

(b) Front, Plasma

(c) Middle, No Plasma

(d) Middle, No Plasma

(e) Back, No Plasma

(f) Back, Plasma

Fig. 6 Sample raw fluorescence images, turbulent boundary layer; flow is from left to right.

B. Laminar Baseline Case

The experiments, while a simplified case of true high-enthalpy hypersonic conditions, combine complex mechanisms, TNE and boundary layer turbulence. For this reason, it is instructive to begin the analysis with the comparatively simple "Laminar, Plasma Off" case and use it as the foundation for deeper analyses of the more challenging tests. The edge-normalized fluorescence signal ratio $\left(\frac{R}{R_e}\right)$ profiles for the "Laminar, Plasma Off" case provided in Fig. 7 show there was little evolution along the plate, the profiles all falling within the overlapping error bars. The slight temperature decay through the freestream was likely due to the plate being installed slightly below the tunnel centerline, the presence of N_xO_y species due to seeding, or some combination thereof [14]. The enhanced decay near the wall was attributed to thermodynamic processes (*vide infra*) or entropy layer effects due to the shock curvature; the latter mechanism seems more probable, as the cavity subsides by the measurement at the "Back" test location.

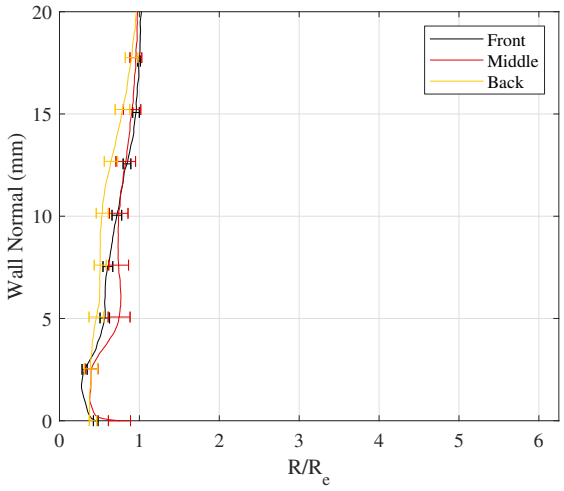

Fig. 7 Edge-normalized fluorescence signal ratio profiles for "Laminar, Plasma Off" case.

It is surprising to observe that although the boundary layer temperature is rising along the plate, $T^v_{NO,\,w} < T^v_{NO,\,e}$. If $T^v_{NO,\,e} = 153.7$ K, one would expect there would be a considerable increase in the temperature. There are several competing theories for this behavior. To begin, it is possible that the early simulation of T^v_{NO} along the nozzle was incorrect and $T^v_{N_2} = T^v_{O_2} = T^v_{NO} = 358$ K. Because $T_w \approx 358$ K [19], this would explain the nearly constant profile through the boundary layer. It is also possible there is complete vibrational slip at the wall. Vibrational slip and its effects on surface pressure and heating has been studied considerably [44–50], mostly with respect to high-temperature shock tube experiments and simulations. Among these works, there is little agreement on predicting a single value for the degree of vibrational slip, though most did not assume complete accommodation. While the conditions in the present experiment, especially the low temperatures and densities, differentiate this analysis from the literature, it is reasonable to expect some amount of vibrational slip at the wall. Partial recovery may explain the slight increase in temperature below $\sim$ 2 mm; however, there was high uncertainty due to the low signal and the rotranslational temperature was

sufficient to enable thermal exchange pathways. In reality, one must assume both mechanisms are happening in tandem, that $T^v_{NO,\,e}$ may be higher than predicted and there is vibrational slip.

Nevertheless, analyzing the thermal kinetic pathways may prove illuminating because if NO is not vibrationally frozen along the plate, it could be equilibrating with N_2 and/or O_2 instead of recovering the wall temperature. The rate constants for the reactions in Table 2, calculated from the "Laminar" simulated rotranslational boundary layer shown in Fig. 4, are provided in Fig. 8(a). Because the source for the data [38] assumed all V-T reactions starting from the same excited base reactant (e.g., $NO^{v=1} + X$) had the same reaction rate constant, only data for the excited species are included. These plots show that as the rotranslational temperature increases near the wall, certain reactions become unfrozen, some increasing at rates dozens of orders of magnitude beyond what occurred in the freestream; again, due to limited available data, these reaction rate constants were used at temperatures below their calibrated range, but the general trends shown are informative. One can observe the dominant reactions: 1) collisional self-quenching of $NO^{v=1}$; 2) $NO^{v=1} \rightarrow O_2^{v=1}$; and 3) $NO^{v=1} \leftarrow O_2^{v=1}$.

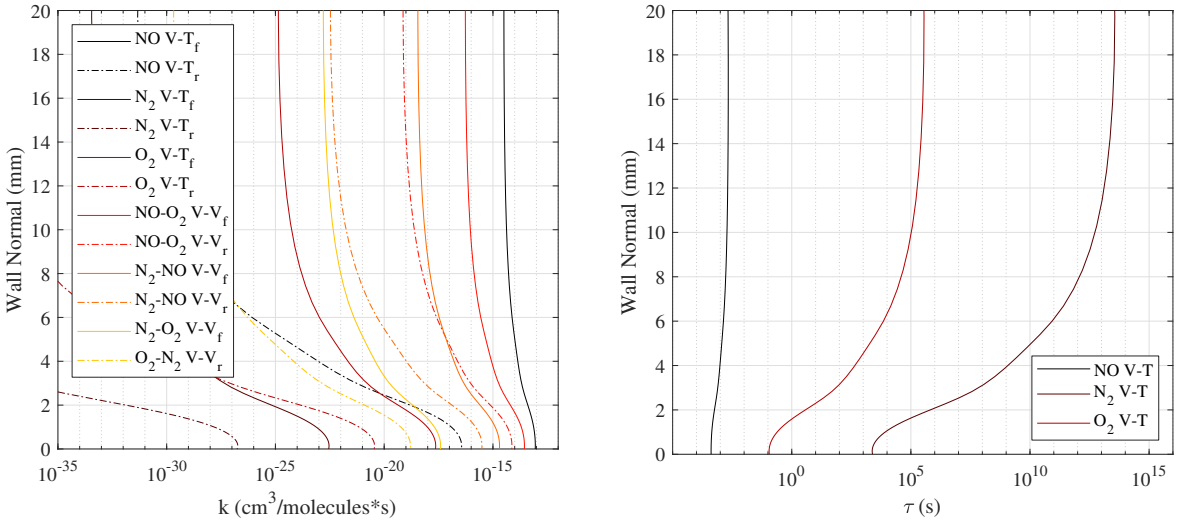

(a) Reaction rate constants.

(b) Landau-Teller constant.

Fig. 8 Thermomechanical processes through a laminar boundary layer at "Front" test location.

The aforementioned results suggest NO could be vibrationally losing energy until one remembers there was > 100 times more O_2 ($\sim$ 21%) in the system than NO ($\sim$0.15%). Thus, there would be orders of magnitude more vibrationally excited O_2 in the boundary layer than NO, even before considering $\theta_{v,O_2} < \theta_{v,NO}$ and that O_2 was likely at some higher vibrational temperature coming out of the nozzle. In other words, even though NO preferentially transferred vibrational energy to O_2, there was more vibrational energy stored in O_2 for the reverse reaction to take place. Finally, there was a significant amount of energy passed from N_2 into NO through the fourth most likely reaction $N_2^{v=1} \rightarrow NO^{v=1}$. All of this, and the no-slip condition at the hot wall, provided a reasonable mechanism for the rise in T^v_{NO} observed.

C. Introduce Turbulent Mixing

The "Turbulent, Plasma Off" data are shown in Fig. 9. The "Front" trace matched the corresponding profile from the laminar dataset, but the other locations did not show the same deficit approaching the wall, the enhanced mixing destroying the trend. The observed wall temperatures matched those from the laminar case.

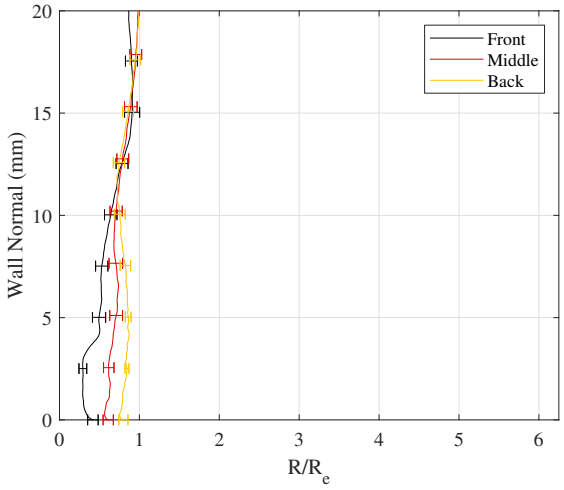

Fig. 9 Edge-normalized fluorescence signal ratio profiles for "Turbulent, Plasma Off" case.

It will be seen that the plasma locally seeded NO into the flow, so proper understanding of diffusion, convection, and mixing is important. The "Laminar" results in Fig. 7 included all but the lattermost effect, implying the vibrational profile expansion with the boundary layer is due to diffusion. The result was a trend toward $T^{v}_{e,\,NO}$ along the test article, but a failure to fully reach it. However, with the introduction of the trips, mixing was effectively "turned on." The result provided in Fig. 9 shows inclusion of these physics allowed the boundary layer to fully recover both the wall and edge conditions. This implies turbulent mixing occurred on a timescale at least as fast as vibrational relaxation.

It is of interest to determine the flow is mechanically frozen, thermally frozen, or if the two mechanisms are on the same timescale and can thereby interact as in Refs. [4, 7]. Even an order-of-magnitude estimate is instructive, and in an effort to characterize this thermodynamic timescale, the Landau-Teller relaxation timescale is used. The form taken here follows Ref. [51] where $\tau_{LT} = \left(N_m k_f \left[1 - \exp\left(-\theta_v/T\right)\right]\right)^{-1}$ where N_m is the number density of the species considered.

The Landau-Teller relaxation timescales were calculated from the CFD results and the data from the laminar case are plotted in Fig. 8(b). It is important to understand these data only represent collisional self-quenching and are limited by the accuracy of the reaction rate constants, but they do provide sufficient trend information in the boundary layer. These calculations suggest N_2 was completely frozen while the relaxation timescales for NO and O_2 were $O(10^{-4})$ and $O(10^{-1}$ s), respectively; these data are consistent with the corresponding rate constants shown in Fig. 8(a). Accounting for the higher concentration of O_2 relative to NO, it is safe to assume $\tau_{LT,NO} = O(10^{-4}s)$ represents the upper limit for the thermodynamic timescale for NO relaxation.

Approximate flow and turbulence timescales originate from a variety of sources. The flow-over-body timescale was $\tau_F = l_{body}/u_e \approx 0.5 \text{ m}/1000 \frac{\text{m}}{\text{s}} \approx 5 \times 10^{-4}$ s; this is a lower-limit, as the streamlines in the boundary layer would take longer to traverse the test article. The large eddy turnover timescale [52] is $\tau_E = \delta/u_e \approx 0.01 \text{ m}/1000 \frac{m}{s} \approx 1 \times 10^{-5}$ s. Calculating the Kolmogorov timescale $\tau_\eta = \sqrt{\nu/\epsilon}$ [52] with the information available required additional modeling. Schetz and Bowersox [53] showed $\epsilon \approx C_D (K^T)^{3/2}/l$ where $C_D \approx 0.09$. Bradshaw et al. [54] provided, for flat plates, $a_1 \rho K^T = \tau_{xy}^T$ where $a_1 = \sqrt{C_D} \approx 0.3$ [55]. Schetz and Bowersox [53] also provided $l_m \approx C_D^{-1/4} l$. If one restricts the analysis to the log layer of an adiabatic flow, which the present flow nearly was (350 K/390.5 K = 0.90 [19]), then $\nu = \nu_w$, $\tau_{xy}^T = \tau_w$, and $l_m \approx \kappa y$ where $\kappa \approx 0.41$ [56]. Recalling the friction velocity $u^* = \sqrt{\tau_w/\rho}$ and assuming the incompressibility ($\rho_w \approx \rho$) yields

$$\epsilon \approx C_D \frac{(K^T)^{\frac{3}{2}}}{l} \approx C_D \frac{(K^T)^{\frac{3}{2}}}{C^{\frac{1}{4}} \kappa y} \approx \frac{C^{\frac{3}{4}}}{\kappa y} \left(\frac{\tau_w}{a_1 \rho} \right)^{\frac{3}{2}} \approx \frac{C^{\frac{3}{4}}}{\kappa a^{\frac{3}{2}}} \frac{(u^*)^3}{y} \approx 2.5 \frac{(u^*)^3}{y}. \tag{3}$$

From the numerical results, $\tau_\eta \approx \sqrt{\frac{\nu}{\epsilon}} \approx 5 \times 10^{-6}$ s. These same simplifications can be applied to the Taylor microscale, the boundary between inertia- and viscosity-dominated regimes [52]. Now $\tau_\lambda = \frac{\lambda}{u'_{RMS}}$ where $\lambda = \left(10 \nu \frac{K^T}{\epsilon} \right)^{\frac{1}{2}}$ can be written $\tau_\lambda \approx \frac{\lambda}{(K^T)^{\frac{1}{2}}} \approx \frac{\left(10 \nu \frac{K^T}{\epsilon} \right)^{\frac{1}{2}}}{(K^T)^{\frac{1}{2}}} \approx \sqrt{10} \tau_\eta \approx 1 \times 10^{-5}$ s.

These results are summarized in Table 3. Initially, the data suggest the flow may be thermally frozen, at least with respect to the turbulent structures, until one remembers the Landau-Teller timescale only considers one reaction at a time and fails to model the entire system. Even if the thermodynamic timescales are one or two orders of magnitude faster, a realistic reduction given the analysis provided above, then there is a high probability the system is thermomechanically coupled. This would open the possibility for complex interactions between the turbulent structures and vibrational energy modes [7]. It must be noted, however, there will be some degree of wall quenching that would act to remove vibrational energy from the system.

Table 3 Approximate thermodynamic and aerodynamic time scales.

$\tau_{LT,NO}$	τ_F	τ_E	τ_η	τ_λ
$< 1 \times 10^{-4}$	$> 5 \times 10^{-4}$	1×10^{-5}	5×10^{-6}	1×10^{-5}

D. Introduce Thermal Nonequilibrium

This section synthesizes the experimental data, thermodynamic relations, and timescales previously discussed. Because each element has been analyzed individually and the theory built one piece at a time, it is now appropriate to push the system by introducing the DC glow discharge plasma. The T_{NO}^v temperature traces measured along the test article are shown in Fig. 10.

Consider first the laminar case, Fig. 10(a). The temperature profiles show the preferential seeding of TNE into

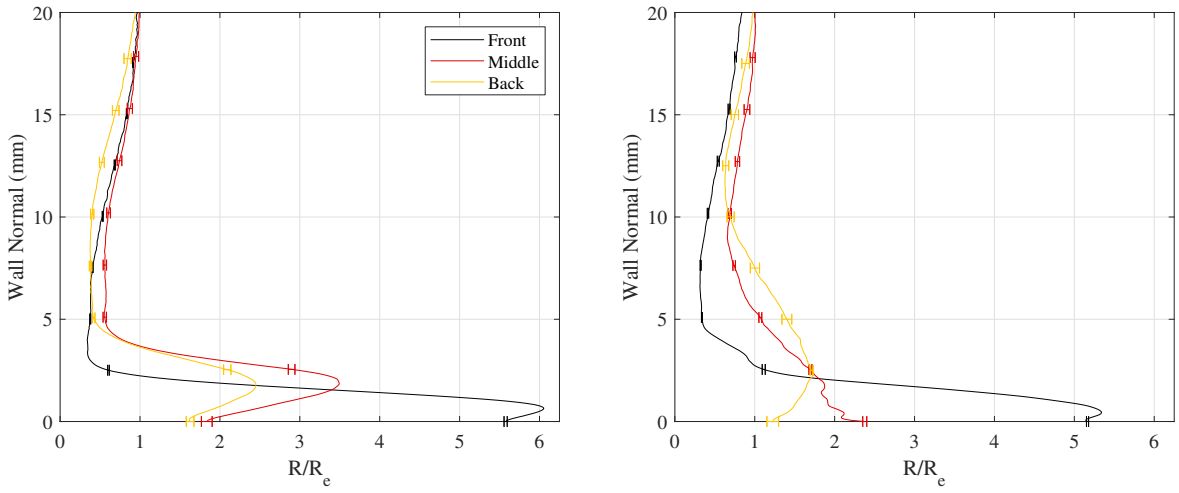

(a) Laminar (b) Turbulent

Fig. 10 Edge-normalized fluorescence signal ratio profiles for "Plasma On" cases; same legend for both figures.

the low-mixing, laminar boundary layer. The observed temperature profile exceeding the freestream temperature demonstrates even at the "Back" test location that the plasma deposited a significant amount of internal energy into the flow and it remained, at least in part, throughout the entire test domain. As shown in Fig. 4, especially in the "Back" test location, laminar boundary layers are thinner and hotter than turbulent boundary layers, which are characterized by rapid temperature decay near the wall [57]. This maintains activated rate constants farther from the wall and thereby more vibrational relaxation to occur. Furthermore, there will be greater velocity reductions meaning there would be more time for said relaxation.

The significance of these results is immediate, as they show comparatively reactive NO was excited by the plasma, but was unable to fully equilibrate to the profiles seen in Fig. 7 by the time the gas traversed the length of the test article. In reality, the plasma was meant to excite N_2, which simply by virtue of being more populous should have contained a larger fraction of the internal energy of the flow. However, because the N_2 was frozen, there could be little tangible effect of vibrational relaxation on the bulk flow. Because no internal energy could be transferred to external states, the energy exchange observed by Fuller et al. [2] could not occur. In addition, no Joule or cathode heating effects were observed [19].

The turbulent data are provided in Fig. 10(b). The effect of the plasma seemed to persist farther into the freestream in the turbulent case than in the laminar case. A likely explanation could be turbulent mixing and diffusion transporting vibrationally hot NO far from the wall, where the low rotranslational temperatures effectively turned off the thermodynamic relaxation processes. Therefore, one could consider two regimes, a thermodynamics-dominated regime near the wall and a turbulence-dominated regime near the freestream. This explains why, by the "Back" test location, the $T^v_{NO,\,e} \approx T^v_{NO,\,w}$ condition seen in the "Plasma Off" profiles of Fig. 9 was recovered, but a clear profile is present at

the edge of the boundary layer where all shape was previously absent. It is noted the temperature rise below $\sim$ 2 mm in the "Middle" test location may be due to the combination of wall thermalization and the temperature peak in the boundary layer rising from the wall between the "Front" and "Back" test locations, but it could also be explained by a dearth of experimental data in this region.

VI. Conclusions

A $\sim$ 47 W DC glow discharge was used to vibrationally excite NO-seeded air in a hypersonic turbulent boundary layer without perturbing the flow. The goal was to collect empirical data relating thermal-mechanical coupling in a canonical, two-temperature environment. These data are intended to inform subsequent TNE models. Modeling of the flow exiting the nozzle implied a three-temperature system where $T^r \neq T^v_{N_2,\,O_2} \neq T^v_{NO}$. This complicated quantitative PLIF temperature measurements. Nevertheless, vibrational pseudotemperature profiles were collected at three locations through the boundary layer using PLIF thermometry. This provided an initial condition for future analyses as well as two test locations along the wedge where simulations could be compared following their evolution along the test article. The results, the first of their kind in a hypersonic boundary layer, were limited to measurement of the ratio of PLIF signals, a temperature-dependent parameter that could provide qualitative and relative measurement of the true vibrational temperature of NO. These data were supported by independent analyses of both thermal and mechanical processes as they pertained to the laminar and turbulent cases, respectively. The case where the plasma was turned on produced conditions where these processes could combine. It is proposed this manifested as a region near the wall where the rotranslational temperature was sufficiently high to allow thermodynamic relaxation of NO. Far from the wall, meanwhile, these processes would freeze and turbulent structures were chiefly responsible for redistributing and mixing the vibrationally excited NO. Capturing such complex thermodynamics in a 3-D, wake-driven, hypersonic turbulent boundary layer would be a challenge for even the most advanced CFD solvers, which underscores the necessity of empirical results like the ones provided herein. Through calibration of $T^v_{NO,\,e}$, future researchers could provide quantitative measurements of T^v_{NO} through the boundary layer and perhaps extend the simple approach to vibrational relaxation demonstrated here for the nozzle to the entire boundary layer.

Acknowledgments

The authors gratefully acknowledge support for this work in part from a grant from the Department of Defense Office of the Under Secretary of Defense (Vannevar Bush Faculty Fellowship Grant Number N00014-18-1-3020) and from RT-3 Vehicle Technologies in the National Aeronautics and Space Administration Hypersonic Technology Project. Its contents are solely the responsibility of the authors and do not necessarily represent the official views of Texas A&M University, the Department of Defense, or the National Aeronautics and Space Administration.

References

[1] Bowersox, R., North, S., and Srinivasan, R., "High-Speed Free Shear Layers with Molecular Non-Equilibrium: An Example of the Fluids Information Triad (Invited)," *AIAA Paper*, Vol. 685, 2008.

[2] Fuller, T. J., Hsu, A. G., Sanchez-Gonzalez, R., Dean, J. C., North, S. W., and Bowersox, R. D., "Radiofrequency plasma stabilization of a low-Reynolds-number channel flow," *Journal of fluid mechanics*, Vol. 748, 2014, pp. 663–691.

[3] Fujii, K., and Hornung, H., "A Procedure to Estimate the Absorption Rate of Sound Propagating Through High Temperature Gas," GALCIT Report FM 2001.004, California Institute of Technology, Pasadena, CA, 8 2001.

[4] Wagnild, R., "High Enthalpy Effects on Two Boundary Layer Disturbances in Supersonic and Hypersonic Flow," Phd thesis, University of Minnesota, Minneapolis, MN, May 2012.

[5] Neville, A. G., Nompelis, I., Subbareddy, P. K., and Candler, G. V., "Effect of thermal non-equilibrium on decaying isotropic turbulence," *AIAA AVIATION 2014-7th AIAA Theoretical Fluid Mechanics Conference 2014*, American Institute of Aeronautics and Astronautics Inc., 2014, p. 3204.

[6] Neville, A. G., Nompelis, I., Subbareddy, P. K., and Candler, G. V., "Thermal non-equilibrium effects in turbulent compressible shear flows," *45th AIAA Fluid Dynamics Conference*, 2015, p. 3218.

[7] Khurshid, S., and Donzis, D. A., "Decaying compressible turbulence with thermal non-equilibrium," *Physics of Fluids*, Vol. 31, No. 1, 2019, p. 015103.

[8] Donzis, D. A., and Maqui, A. F., "Statistically steady states of forced isotropic turbulence in thermal equilibrium and non-equilibrium," *Journal of Fluid Mechanics*, Vol. 797, 2016, pp. 181–200.

[9] Nishihara, M., Takashima, K., Jiang, N., Lempert, W., Adamovich, I., Rich, J., Doraiswamy, S., and Candler, G., "Development of a Mach 5 nonequilibrium-flow wind tunnel," *AIAA journal*, Vol. 50, No. 10, 2012, pp. 2255–2267.

[10] Montello, A., Nishihara, M., Rich, J. W., Adamovich, I., and Lempert, W., "Picosecond USED-CARS for simultaneous rotational/translational and vibrational temperature measurement of nitrogen in a nonequilibrium Mach 5 flow," *50th AIAA Aerospace Sciences Meeting including the New Horizons Forum and Aerospace Exposition*, 2012, p. 239.

[11] Semper, M., Tichenor, N., Bowersox, R., Srinvasan, R., and North, S., "On the design and calibration of an actively controlled expansion hypersonic wind tunnel," *47th AIAA Aerospace Sciences Meeting including The New Horizons Forum and Aerospace Exposition*, 2009, p. 799.

[12] Tichenor, N., Semper, M., Bowersox, R., Srinvasan, R., and North, S., "Calibration of an actively controlled expansion hypersonic wind tunnel," *27th AIAA Aerodynamic Measurement Technology and Ground Testing Conference*, 2010, p. 4793.

[13] Buen, Z. D., Broslawski, C., Smotzer, M., Kuszynski, J. E., North, S., and Bowersox, R. D., "Towards Vibrationally Excited Nitric Oxide Monitoring (VENOM) in a Laminar, Hypersonic Boundary Layer," *AIAA Scitech 2020 Forum*, 2020, p. 1275.

[14] Buen, Z. D., "Implementation of NO LIF Diagnostics to Characterize the Role of Thermal Non-Equilibrium within a Hypersonic Turbulent Boundary Layer," Phd thesis, Texas A&M University, College Station, TX, November 2021.

[15] John, J. E., and Keith, T. G., *Gas Dynamics*, 3rd ed., Pearson Prentice-Hall, 2006.

[16] Semper, M., "Examining a Hypersonic Turbulent Boundary Layer at Low Reynolds Number," phdthesis, Texas A&M University, 8 2013.

[17] Leidy, A. N., "An Experimental Characterization of 3-D Transitional Shock Wave Boundary Layer Interactions at Mach 6." phdthesis, Texas A&M University, 5 2019.

[18] Dwivedi, A., Broslawski, C. J., Candler, G. V., and Bowersox, R. D., "Three-dimensionality in shock/boundary layer interactions: a numerical and experimental investigation," *AIAA AVIATION 2020 FORUM*, 2020, p. 3011.

[19] Broslawski, C., Morreale, B., Bowersox, R. D., Nicholson, G., and Duan, L., "Further Validation and Implementation of an Algebraic Energy Flux Model for High Speed Gaseous Shear Flows," *AIAA SCITECH 2022 Forum*, 2022, p. 0340.

[20] Cohen, C. B., and Reshotko, E., "Similar solutions for the compressible laminar boundary layer with heat transfer and pressure gradient," Tech. rep., National Advisory Committee for Aeronautics, 1955.

[21] Saric, W. S., Reed, H. L., and Kerschen, E. J., "Boundary-layer receptivity to freestream disturbances," *Annual review of fluid mechanics*, Vol. 34, 2002, p. 291.

[22] Hanson, R. E., Buckley, H. P., and Lavoie, P., "Aerodynamic optimization of the flat-plate leading edge for experimental studies of laminar and transitional boundary layers," *Experiments in fluids*, Vol. 53, No. 4, 2012, pp. 863–871.

[23] Menart, J., Shang, J., Kimmel, R., and Hayes, J., "Effects of magnetic fields on plasmas generated in a Mach 5 wind tunnel," *34th AIAA Plasmadynamics and Lasers Conference*, 2003, p. 4165.

[24] Shang, J., Kimmel, R., Hayes, J., Tyler, C., and Menart, J., "Hypersonic experimental facility for magnetoaerodynamic interactions," *Journal of Spacecraft and Rockets*, Vol. 42, No. 5, 2005, pp. 780–789.

[25] Kimmel, R. L., Hayes, J. R., Menart, J. A., and Shang, J., "Effect of magnetic fields on surface plasma discharges at Mach 5," *Journal of spacecraft and rockets*, Vol. 43, No. 6, 2006, pp. 1340–1346.

[26] Shang, J., Surzhikov, S., Kimmel, R., Gaitonde, D., Menart, J., and Hayes, J., "Mechanisms of plasma actuators for hypersonic flow control," *Progress in Aerospace Sciences*, Vol. 41, No. 8, 2005, pp. 642–668.

[27] Shang, J., and Surzhikov, S. T., "Magnetoaerodynamic actuator for hypersonic flow control," *AIAA journal*, Vol. 43, No. 8, 2005, pp. 1633–1652.

[28] Menart, J., Stanfield, S., Shang, J., Kimmel, R., and Hayes, J., "Study of plasma electrode arrangements for optimum lift in a Mach 5 flow," *44th AIAA aerospace sciences meeting and exhibit*, 2006, p. 1172.

[29] Shang, J. S., Kimmel, R. L., Menart, J., and Surzhikov, S. T., "Hypersonic flow control using surface plasma actuator," *Journal of Propulsion and Power*, Vol. 24, No. 5, 2008, pp. 923–934.

[30] Houpt, A., Hedlund, B., Leonov, S., Ombrello, T., and Carter, C., "Quasi-DC electrical discharge characterization in a supersonic flow," *Experiments in Fluids*, Vol. 58, No. 4, 2017, pp. 1–17.

[31] Raizer, Y. P., *Gas discharge physics*, Vol. 1, Springer, 1991.

[32] Roth, J., "Industrial Plasma Engineering Volume 1 Principles. Bristol and Philadelphia," *Institute of Physics publishing*, 1995.

[33] Lieberman, M. A., and Lichtenberg, A. J., *Principles of plasma discharges and materials processing*, John Wiley & Sons, 2005.

[34] Berry, S. A., Auslender, A. H., Dilley, A. D., and Calleja, J. F., "Hypersonic boundary-layer trip development for Hyper-X," *Journal of Spacecraft and Rockets*, Vol. 38, No. 6, 2001, pp. 853–864.

[35] McManamen, B. T., "Velocity and Temperature Measurements in a High Mach Number Shock-Turbulence Interaction," Phd thesis, Texas A&M University, College Station, TX, August 2019.

[36] Seitzman, J. M., and Hanson, R. K., *Planar Fluorescence Imaging in Gases*, Academic Press, 1993, Chap. 6, pp. 406–466.

[37] Hsu, A. H., "Application of Advanced Laser and Optical Diagnostics Towards Non-Thermochemical Equilibrium Systems," phdthesis, Texas A&M University, 2009.

[38] Candler, G. K., J.D., M., and M.N., I., Adamovich, "Vibrational excitation, thermal nonuniformities, and unsteady effects on supersonic blunt bodies," *AIAA journal*, Vol. 40, No. 9, 2002, pp. 1803–1810.

[39] Herzberg, G., *Molecular spectra and molecular structure: I: Spectra of diatomic molecules*, Vol. 1, Van Nostrand, 1950.

[40] Candler, G. V., Johnson, H. B., Nompelis, I., Gidzak, V. M., Subbareddy, P. K., and Barnhardt, M., "Development of the US3D code for advanced compressible and reacting flow simulations," *53rd AIAA Aerospace Sciences Meeting*, 2015, p. 1893.

[41] Ames Research Staff, "Equations, tables, and charts for compressible flow," Tech. Rep. NACA-TR-1135, National Advisory Committee for Aeronautics, January 1953.

[42] Spalart, P., and Allmaras, S., "A one-equation turbulence model for aerodynamic flows," *30th aerospace sciences meeting and exhibit*, 1992, p. 439.

[43] Smits, A. J., and Martin, M. P., "Turbulence in supersonic and hypersonic boundary layers10282," *IUTAM Symposium on One Hundred Years of Boundary Layer Research*, Springer, 2006, pp. 221–230.

[44] Nompelis, I., Candler, G. V., and Holden, M. S., "Effect of vibrational nonequilibrium on hypersonic double-cone experiments," *AIAA journal*, Vol. 41, No. 11, 2003, pp. 2162–2169.

[45] Sauerwein, R. H. B., "Influence of molecular vibrational energy accommodation modeling on cone surface heat flux at mach 10," *David Publishing Company www. davidpublisher. com*, Vol. 10, 2016, pp. 660–666.

[46] Yu, Y.-L., Li, X.-D., Wang, Z.-H., and Bao, L., "Theoretical modeling of heat transfer to flat plate under vibrational excitation freestream conditions," *International Journal of Heat and Mass Transfer*, Vol. 151, 2020, p. 119434.

[47] Boyd, I., Phillips, W., Levin, D., Boyd, I., Phillips, W., and Levin, D., "Sensitivity studies for prediction of ultra-violet radiation in nonequilibrium hypersonic bow-shock waves," *35th Aerospace Sciences Meeting and Exhibit*, 1997, p. 131.

[48] Black, G., Wise, H., Schechter, S., and Sharpless, R. L., "Measurements of vibrationally excited molecules by Raman scattering. II. Surface deactivation of vibrationally excited N2," *The Journal of Chemical Physics*, Vol. 60, No. 9, 1974, pp. 3526–3536.

[49] Moss, J. N., and Bird, G. A., "Direct simulation Monte Carlo simulations of hypersonic flows with shock interactions," *AIAA journal*, Vol. 43, No. 12, 2005, pp. 2565–2573.

[50] Méolans, J., "Thermal slip boundary conditions in vibrational nonequilibrium flows," *Mechanics Research Communications*, Vol. 30, No. 6, 2003, pp. 629–637.

[51] Park, C., *Nonequilibrium hypersonic aerothermodynamics*, Wiley, 1990.

[52] Pope, S. B., *Turbulent Flows*, Cambridge University Press, 2015.

[53] Schetz, J. A., and Bowersox, R. D., *Boundary layer analysis*, American Institute of Aeronautics and Astronautics, 2011.

[54] Bradshaw, P., Ferriss, D., and Atwell, N., "Calculation of boundary-layer development using the turbulent energy equation," *Journal of Fluid Mechanics*, Vol. 28, No. 3, 1967, pp. 593–616.

[55] Keating, A., De Prisco, G., and Piomelli, U., "Interface conditions for hybrid RANS/LES calculations," *International journal of heat and fluid flow*, Vol. 27, No. 5, 2006, pp. 777–788.

[56] Coles, D., "The law of the wake in the turbulent boundary layer," *Journal of Fluid Mechanics*, Vol. 1, No. 2, 1956, pp. 191–226.

[57] White, F. M., *Viscous fluid flow*, 3rd ed., McGraw-Hill, 2006.